Original articles

Modeling and computation of real-time applied torques and non-holonomic constraint forces/moment, and optimal design of wheels for an autonomous security robot tracking a moving target

Chu Anh My[a],*, Stanislav S. Makhanov[b], Nguyen A. Van[a], Vu M. Duc[a]

[a] *Department of Special Robotics and Mechatronics, Le Quy Don Technical University, 236 Hoang Quoc Viet, Hanoi, Viet Nam*
[b] *School of Information and Computer Technology, Sirindhorn International Institute of Technology, Thammasat University, Tiwanont Road, T. Bangkadi, A. Muang, Pathum Thani 12000, Thailand*

Abstract

The paper presents a new mathematical model to analyze real time applied torques and non-holonomic constraint forces/moment of a security robot, comprised of a wheeled mobile platform and a manipulator for special security task applications. Based on the analysis the optimal selection of the wheels of the robot can be performed so that the slippage on the surface has been minimized. The proposed analysis constitutes a novel component in the modeling and design of the security robots. Numerical experiments illustrate the efficiency of the proposed method.

© 2019 International Association for Mathematics and Computers in Simulation (IMACS). Published by Elsevier B.V. All rights reserved.

1. Introduction

Consider an autonomous security robot system tracking a target depicted in Fig. 1. In a spectrum of real security task situations, the robot is required to follow a given path $\mathbf{r}(u(t)) = \begin{bmatrix} x_r(u(t)) & y_r(u(t)) \end{bmatrix}^T$ with the desired velocity $\dot{s}(t)$, where t is the time and $u(t) \in [0, 1]$ the normalizing parameter. Meanwhile, the end-effector (end of the robotic arm) must track and aim the target which travels along a path $\mathbf{c}(u(t)) = \begin{bmatrix} x_c(u(t)) & y_c(u(t)) \end{bmatrix}^T$ at a velocity $\dot{l}(t)$.

This functional requirement can be formulated as follows

$$\begin{bmatrix} x_P(t) & y_P(t) \end{bmatrix}^T = \begin{bmatrix} x_r(u(t)) & y_r(u(t)) \end{bmatrix}^T,$$

$$\mathbf{v}_r(t) = \dot{s}(t)\,\mathbf{T}_r(t),$$

where $(x_P(t), y_P(t))$ is the position of the platform, $\mathbf{v}_r(t)$ the linear velocity and $\mathbf{T}_r(t)$ the tangential vector to the curve $\mathbf{r}(u(t))$.

---

* Corresponding author.
E-mail addresses: mychuanh@yahoo.com (C.A. My), makhanov@siit.tu.ac.th (S.S. Makhanov), vank24hv@gmail.com (N.A. Van), minhducvu2009@yahoo.com (V.M. Duc).
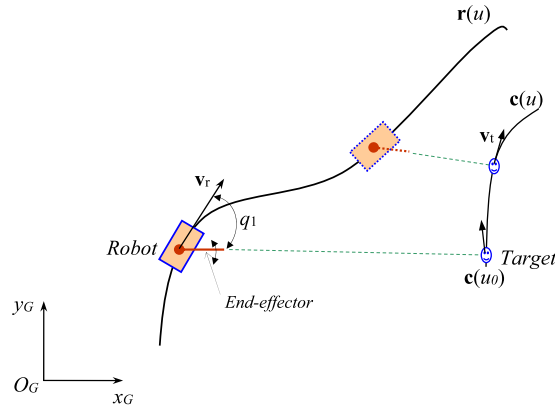
Fig. 1. The robot system and the target.

It should be noted that integration of the modular manipulator on the platform and the requirement of the non-slip rolling of the wheels on the surface is subjected to the non holonomic constraints and the redundancy. Therefore, the modeling and analysis of such systems requires mathematical and numerical analysis.

A number of research papers analyze the dynamics of the general mobile manipulators. Qing and I-Ming [22] derive the governing equations, Wronka and Dunnigan [26] develop dynamic equations for the case when a two degree of freedom platform floats on the water, Liu and Li [15] consider a platform which moves on a sloping surface. Padois et al. [19] provide a unified description of the kinematic and dynamic model of the manipulator. Bayar et al. [2] investigate the dynamic modeling and parameter estimation for traction, rolling, and lateral wheel forces to enhance mobile robot trajectory tracking. Akli et al. [1] analyze the motion of a mobile manipulator executing pick-up tasks. Tounsi and Le Corre [25] propose a method of calculation of a complex smooth path to minimize the integral-square-jerk for a mobile robot. A general framework for the feedback control is proposed by Fruchard et al. [5]. Strategies of robust force/motion control and trajectory tracking are presented by Li et al. [13], Dong [4], Mazur [17], and Mailah et al. [16]. Tan et al. [24] integrate the task planning into the control strategy of the robot. Galicki [6] solves the problem of the end-effector trajectory tracking problem subject to the state equality and inequality constraints. Galicki [7,8] offer solutions to positioning of the end-effector with the mobile manipulator subjected to constraints. The solution is based on the Lyapunov stability theory combined with the penalty function approach. Korayem and Shafei [12] present a symbolic algorithm, capable of deriving equations of motion of n-rigid linked manipulators with revolute-prismatic joints mounted on a mobile platform. The equations of motion have been derived using the Gibbs–Appell formulation which avoids the Lagrange multipliers associated with the nonholonomic constraints. Khalil and Moosavian [11] consider a mobile manipulator of heavy objects. Based on the dynamic equations, the motion of the moving base is planned so that the stability of the entire system is guaranteed. Joanna and Krzysztof [10] propose dynamically consistent Jacobian inverse kinematics techniques to control the mobile manipulators. Dietrich et al. [3] investigate a whole-body impedance control for wheeled mobile manipulators. Mishra et al. [18] use a nonlinear control with an uncertainty estimator for robust task-space motion control of a mobile manipulator. Wu et al. [27] present a robust adaptive sliding-mode control scheme for a class of condenser-cleaning mobile manipulator in the presence of parametric uncertainties and external disturbances. Peng et al. [20] study a robust adaptive tracking control for a nonholonomic mobile manipulator with uncertainties. Xia et al. [28] propose an effective tracking control method based on fuzzy neural network and extended Kalman filter for a wheeled mobile manipulator. Rigatos [23] summarizes the basics of the Extended Kalman Filter, which is the most popular approach to implement sensor fusion in mobile robot control. Izumi and Watanabe [9] construct a method for the intelligent control system of a mobile robot using the fuzzy behavior-based control. It is clearly seen that though the several methods and techniques have been investigated for the dynamic modeling, analysis and control for mobile robots and mobile manipulators, little attention has been paid to the dynamic modeling and the real time dynamic analysis for a mobile manipulator, of which the mobile platform is required to travel along a freeform curve meanwhile the manipulator points to a stationary/moving target. To the best of our knowledge, the analysis of the real time applied torques and non-holonomic constraint of the described robotic system has been
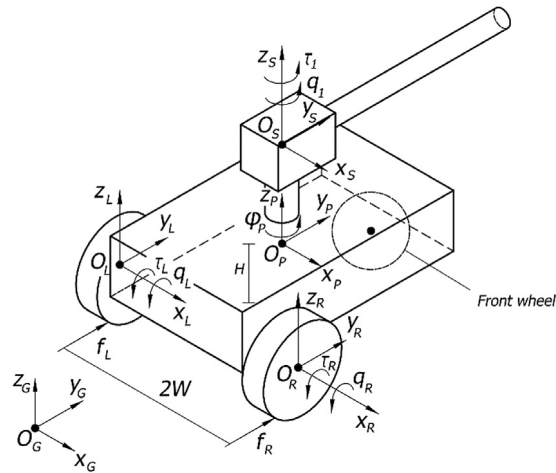
Fig. 2. The robot system model.

overlooked. Nevertheless, such analysis provides an important basis for the stability of the robot, improvement of the control quality and selection of actuators and wheels.

Therefore, the paper presents a methodology to model and analyze the set of torques and non-holonomic constraint forces applied on the robot. Based on the dynamic model represented in the minimal form, the non-holonomic constraints have been coupled with the differential equations of motion. Furthermore, the conventional Lagrangian multipliers have been eliminated. The closed form solution for torques and forces have been derived for two cases: the target is moving and the target is stationary. The non-holonomic constraint forces involving the static sliding friction force have been included into the solution. The conditions of slipless motion and the corresponding friction coefficients are discussed in detail. The results present a theoretical framework for optimizing the design of wheels with respect to the functional requirements of the system as well as the environmental conditions (friction).

2. Dynamic modeling

The mobile platform is designed with two active wheels of the radius R in the rear and one passive caster wheel in front. The end-effector module is mounted on the platform via a revolute joint. In other words, the system consists of four bodies: the left wheel (1), the right wheel (2), the main platform body (3), and the end-effector (4). We assume that (i) the mass of the passive wheel is much smaller than the mass of the entire system, and therefore does not have any impact in the dynamics, (ii) all bodies of the system are rigid, (iii) the ground surface the robot moves on is flat.

The model of the security robot system is depicted in Fig. 2, where $O_G = (O_G, x_G, y_G, z_G)$ is the reference frame, (x_G, y_G) belong to the ground surface, $O_p = (O_p, x_p, y_p, z_p)$ is the mobile platform coordinate system. The origin is the center of mass, x_p is parallel to the center line connecting the centers of the rear wheels, y_p axis points toward the head, and the plane $O_p x_p y_p$ is parallel to $O_G x_G y_G$.

Finally, $O_L = (O_L, x_L, y_L, z_L)$ and $O_R = (O_R, x_R, y_R, z_R)$ the left and the right wheel coordinate system respectively whereas $O_S = (O_S, x_S, y_S, z_S)$ is the end-effector coordinate system, where the origin is the center of the revolute joint by which the end-effector connects onto the platform.

We assume that at $t = 0$, x_S is parallel to x_p, and z_S is parallel to z_p.

Let $\mathbf{q}_w = \begin{bmatrix} q_L & q_R \end{bmatrix}^T$ be the vector of the rolling angles of the left and the right wheel, respectively and $\mathbf{q} = \begin{bmatrix} q_L & q_R & q_1 \end{bmatrix}^T$ the vector of minimal generalized coordinates, where q_1 is the rotation angle of the end-effector with respect to the platform. Furthermore, $\mathbf{q}_e = \begin{bmatrix} q_L & q_R & x_P & y_P & \varphi_P & q_1 \end{bmatrix}^T$ denotes the extended generalized coordinates, where x_P, y_P and φ_P are the position and the orientation of the platform in O_G. Finally, τ_L, τ_R and τ_1 denote the torques applied to the left wheel, the right wheel and the end-effector, respectively.

The multi-body approach implies that the position and orientation of each body is characterized by the coordinates of the center of mass $\mathbf{r}_{Gi}$ and the rotation matrix $\mathbf{A}_{Gi}$, $i = 1, 2, 3, 4$ in the reference frame O_G. Thus, the absolute

angular velocity $\boldsymbol{\omega}_{Gi}$, the translational Jacobian matrix $\mathbf{J}_{Ti}$ and the rotational Jacobian matrix $\mathbf{J}_{Ri}$ are respectively given by

$$\tilde{\boldsymbol{\omega}}_{Gi} = \dot{\mathbf{A}}_{Gi}\mathbf{A}_{Gi}^{T}, \tag{1}$$

$$\mathbf{J}_{Ti} = \frac{\partial \mathbf{r}_{Gi}}{\partial \mathbf{q}_e}, \tag{2}$$

$$\mathbf{J}_{Ri} = \frac{\partial \boldsymbol{\omega}_{Gi}}{\partial \dot{\mathbf{q}}_e}, \tag{3}$$

where $\tilde{\boldsymbol{\omega}}_{Gi}$ denotes the skew matrix.

The generalized mass matrix of the system is then

$$\mathbf{M}(\mathbf{q}_e) = \sum_{i=1}^{4} m_i \mathbf{J}_{Ti}^{T} \mathbf{J}_{Ti} + \mathbf{J}_{Ri}^{T} \mathbf{I}_i \mathbf{J}_{Ri}, \tag{4}$$

where m_i and $\mathbf{I}_i$ is the mass and the linear inertia moment of the ith body, respectively.

The equations of motion complemented by the non-holonomic constraints are given by

$$\begin{cases} \mathbf{M}(\mathbf{q}_e)\ddot{\mathbf{q}}_e + \mathbf{C}(\mathbf{q}_e, \dot{\mathbf{q}}_e)\dot{\mathbf{q}}_e + \mathbf{G}(\mathbf{q}_e) = \boldsymbol{\tau}_e + \mathbf{A}^{T}(\mathbf{q}_e)\boldsymbol{\lambda}, \\ \mathbf{A}(\mathbf{q}_e)\dot{\mathbf{q}}_e = 0, \end{cases} \tag{5}$$

where the Coriolis matrix $\mathbf{C}(\mathbf{q}_e, \dot{\mathbf{q}}_e)$ satisfies

$$\mathbf{C}(\mathbf{q}_e, \dot{\mathbf{q}}_e) = \frac{\partial \mathbf{M}}{\partial \mathbf{q}_e}(\mathbf{E}_{6x6} \otimes \mathbf{q}_e) - \frac{1}{2}\left(\frac{\partial \mathbf{M}}{\partial \mathbf{q}_e}(\mathbf{q}_e \otimes \mathbf{E}_{6x6})\right)^{T}. \tag{6}$$

Finally, the generalized force $\mathbf{G}(\mathbf{q}_e)$ is evaluated by

$$\mathbf{G} = \left(\frac{\partial \Pi}{\partial \mathbf{q}_e}\right)^{T}, \tag{7}$$

where $\Pi = \sum_{i=1}^{4} m_i \mathbf{g}^{T} \mathbf{r}_{Gi}$ is the potential energy of the system.

Define the extended vector of the generalized torques $\boldsymbol{\tau}_e = \begin{bmatrix} \tau_L & \tau_R & 0 & 0 & 0 & \tau_1 \end{bmatrix}^{T}$. Note that number of the components of $\boldsymbol{\tau}_e$ equals to the number of components of the extended generalized coordinate vector.

Let $\boldsymbol{\lambda} = \begin{bmatrix} \lambda_1 & \lambda_2 & \lambda_3 \end{bmatrix}^{T}$ be the vector of the Lagrangian multipliers λ_i.

The non-holonomic constraint equation

$$\begin{bmatrix} \dot{x}_P \\ \dot{y}_P \\ \dot{\varphi}_P \end{bmatrix} = \begin{bmatrix} \dfrac{R\sin(\varphi_P)}{2} & \dfrac{R\sin(\varphi_P)}{2} \\ -\dfrac{R\cos(\varphi_P)}{2} & -\dfrac{R\cos(\varphi_P)}{2} \\ \dfrac{R}{W} & -\dfrac{R}{W} \end{bmatrix} \begin{bmatrix} \dot{q}_L \\ \dot{q}_R \end{bmatrix} \tag{8}$$

implies that the matrix of the non-holonomic constraint is given by

$$\mathbf{A}(\mathbf{q}_e) = \begin{bmatrix} \dfrac{R\sin\varphi_P}{2} & \dfrac{R\sin\varphi_P}{2} & -1 & 0 & 0 & 0 \\ -\dfrac{R\cos\varphi_P}{2} & -\dfrac{R\cos\varphi_P}{2} & 0 & -1 & 0 & 0 \\ \dfrac{R}{W} & -\dfrac{R}{W} & 0 & 0 & -1 & 0 \end{bmatrix}.$$

Note that Eq. (8) is based on the condition that the wheels move on the surface without slip. Finally, (5)–(8) is a nonlinear system of ODE of the second order. Furthermore, we eliminate $\boldsymbol{\lambda}$ and $\mathbf{q}_e$ as follows.

First, denote

$$\mathbf{S}\left(\mathbf{q}_e\right) = \begin{bmatrix} 1 & 0 & 0 \\ 0 & 1 & 0 \\ \dfrac{R\sin(\varphi_P)}{2} & \dfrac{R\sin(\varphi_P)}{2} & 0 \\ -\dfrac{R\cos(\varphi_P)}{2} & -\dfrac{R\cos(\varphi_P)}{2} & 0 \\ \dfrac{R}{W} & -\dfrac{R}{W} & 0 \\ 0 & 0 & 1 \end{bmatrix}. \tag{9}$$

Therefore,

$$\dot{\mathbf{q}}_e = \mathbf{S}\left(\mathbf{q}_e\right)\dot{\mathbf{q}}, \tag{10}$$

$$\mathbf{A}\left(\mathbf{q}_e\right)\mathbf{S}\left(\mathbf{q}_e\right) = \mathbf{0}. \tag{11}$$

Hence

$$\mathbf{S}^T\left(\mathbf{q}_e\right)\mathbf{A}^T\left(\mathbf{q}_e\right) = \mathbf{0}. \tag{12}$$

Differentiating Eq. (10) yields

$$\ddot{\mathbf{q}}_e = \mathbf{S}\left(\mathbf{q}_e\right)\ddot{\mathbf{q}} + \dot{\mathbf{S}}\left(\mathbf{q}_e\right)\dot{\mathbf{q}}. \tag{13}$$

Invoking $\mathbf{A}\left(\mathbf{q}_e\right)\dot{\mathbf{q}}_e = 0$, multiplying Eq. (5) by $\mathbf{S}^T\left(\mathbf{q}_e\right)$, and substituting Eqs. (13) and (14) reveals that

$$\mathbf{S}^T\mathbf{M}\mathbf{S}\ddot{\mathbf{q}} + \mathbf{S}^T\left(\mathbf{M}\dot{\mathbf{S}} + \mathbf{C}\mathbf{S}\right)\dot{\mathbf{q}} + \mathbf{S}^T\mathbf{G} = \mathbf{S}^T\boldsymbol{\tau}_e. \tag{14}$$

After some algebraic manipulations we have

$$\mathbf{M}_n\left(\mathbf{q}_e\right)\ddot{\mathbf{q}} + \mathbf{C}_n\left(\mathbf{q}_e, \dot{\mathbf{q}}_e\right)\dot{\mathbf{q}} + \mathbf{G}_n\left(\mathbf{q}_e\right) = \mathbf{Q}_n, \tag{15}$$

where $\mathbf{M}_n = \mathbf{S}^T\mathbf{M}\mathbf{S}$, $\mathbf{C}_n = \mathbf{S}^T(\mathbf{M}\dot{\mathbf{S}} + \mathbf{C}\mathbf{S})$, $\mathbf{G}_n = \mathbf{S}^T\mathbf{G}$, $\mathbf{Q}_n = \mathbf{S}^T\boldsymbol{\tau}_e = \boldsymbol{\tau}$, and $\boldsymbol{\tau} = [\tau_L \quad \tau_R \quad \tau_1]^T$.

Combining the above relationships yields the following result

$$\begin{cases} \mathbf{M}_n\left(\mathbf{q}_e\right)\ddot{\mathbf{q}} + \mathbf{C}_n\left(\mathbf{q}_e, \dot{\mathbf{q}}_e\right)\dot{\mathbf{q}} + \mathbf{G}_n\left(\mathbf{q}_e\right) = \boldsymbol{\tau}, \\ \mathbf{A}\left(\mathbf{q}_e\right)\dot{\mathbf{q}}_e = 0. \end{cases} \tag{16}$$

Observe that Eqs. (16) represent the so-called minimal form which does not involve the constraint forces. Instead, the generalized coordinates $\mathbf{q}_e$ and $\dot{\mathbf{q}}_e$ are included coefficients of the first equation.

3. Real time applied torques analysis

In order to calculate the torque $\boldsymbol{\tau}(t) = [\tau_L(t) \quad \tau_R(t) \quad \tau_1(t)]^T$ the variables $\mathbf{q}(t)$, $\dot{\mathbf{q}}(t)$, $\ddot{\mathbf{q}}(t)$, $\mathbf{q}_e(t)$, $\dot{\mathbf{q}}_e(t)$, as well as the coefficients $\mathbf{M}_n\left(\mathbf{q}_e(t)\right)$, $\mathbf{C}_n\left(\mathbf{q}_e(t), \dot{\mathbf{q}}_e(t)\right)$, $\mathbf{G}_n\left(\mathbf{q}_e(t)\right)$ must be evaluated subject to the available constraints. As stated before, the mobile platform moves along $\mathbf{r}(t)$ with the required velocity $\mathbf{v}_r(t)$, while the target is either stationary or moving along $\mathbf{c}(t)$ with the velocity $\mathbf{v}_t(t)$. Besides, $q_1(t)$ is being changed continuously so that the end-effector always aims to the target.

Furthermore, the movement of the platform implies that the origin the coordinate system O_p is being translated along $\mathbf{r}(t)$. At every point $\mathbf{r}(t)$ the linear velocity vector $\mathbf{v}_r(t)$ is collinear with the axis Y_p (coordinate system O_p) and the unit tangent vector $\mathbf{T}_r(t) = \frac{\dot{\mathbf{r}}(t)}{|\dot{\mathbf{r}}(t)|}$.

Observe that the trajectories of the robot and the target must be planned based on the prescribed geometric paths $\mathbf{r}(u)$, $\mathbf{c}(u)$ and the velocity profiles.

Denote $\dot{s}(t) = |\mathbf{v}_r(t)|$ and $\dot{l}(t) = |\mathbf{v}_t(t)|$. The curves $\mathbf{r}(t) = \begin{bmatrix} x_r(t) & y_r(t) \end{bmatrix}^T$ and $\mathbf{c}(t) = \begin{bmatrix} x_c(t) & y_c(t) \end{bmatrix}^T$ are obtained using interpolation (such as the Bezier splines) and the arc-length re-parametrization, where the arc length $s(t) = \int \dot{s}(t)\,dt$.

Since the wheels roll on the surface without slip, the linear and angular velocity of the platform are given by

$$\dot{s}(t) = \frac{R\left[\dot{q}_L(t) + \dot{q}_R(t)\right]}{2}, \tag{17}$$

$$\frac{\dot{s}(t)}{\rho_r(t)} = \frac{R\left[\dot{q}_L(t) - \dot{q}_R(t)\right]}{2W}, \tag{18}$$

where $\rho_r(t) = \frac{|\dot{\mathbf{r}}(t)|^3}{|\dot{\mathbf{r}}(t) \times \ddot{\mathbf{r}}(t)|}$ is the curvature radius of $\mathbf{r}(t)$.

Therefore,

$$\begin{bmatrix} \dot{q}_L(t) \\ \dot{q}_R(t) \end{bmatrix} = \begin{bmatrix} \dfrac{1}{R} + \dfrac{W}{R\rho_r(t)} \\ \dfrac{1}{R} - \dfrac{W}{R\rho_r(t)} \end{bmatrix} \dot{s}(t). \tag{19}$$

Eq. (20) establishes the relationship between the velocity of the wheels, $\dot{\mathbf{q}}_w(t)$ and the linear velocity of the platform $\dot{s}(t)$. Note that our numerical algorithm employs

$$\mathbf{q}_w(t) = \mathbf{q}_w(0) + \int_0^t \dot{\mathbf{q}}_w(\zeta)\, d\zeta. \tag{20}$$

Differentiating Eq. (20) yields

$$\begin{bmatrix} \ddot{q}_L(t) \\ \ddot{q}_R(t) \end{bmatrix} = \begin{bmatrix} -\dfrac{W\dot{\rho}_r}{R\rho_r^2} & \dfrac{1}{R} + \dfrac{W}{R\rho_r} \\ \dfrac{W\dot{\rho}_r}{R\rho_r^2} & \dfrac{1}{R} - \dfrac{W}{R\rho_r} \end{bmatrix} \begin{bmatrix} \dot{s}(t) \\ \ddot{s}(t) \end{bmatrix}. \tag{21}$$

At time t the coordinates of the target and the platform are respectively $\mathbf{c}(t)$ and $\mathbf{r}(t)$. Hence the angle between $\mathbf{T}_r(t)$ and $\mathbf{c}(t) - \mathbf{r}(t)$, is given by

$$q_1(t) = \cos^{-1}\left(\frac{\mathbf{T}_r(t)(\mathbf{c}(t) - \mathbf{r}(t))}{|\mathbf{c}(t) - \mathbf{r}(t)|}\right). \tag{22}$$

Furthermore, the minimal generalized coordinates $\mathbf{q}(t) = \begin{bmatrix} q_L(t) & q_R(t) & q_1(t) \end{bmatrix}^T$ and their derivatives are evaluated from Eqs. (21)–(23).

Note that

$$\begin{bmatrix} x_P(t) & y_P(t) \end{bmatrix}^T = \begin{bmatrix} x_r(t) & y_r(t) \end{bmatrix}^T, \tag{23}$$

$$\varphi_P(t) = -\arctan\left(\frac{\dot{x}_p(t)}{\dot{y}_p(t)}\right), \tag{24}$$

$$\begin{bmatrix} \dot{x}_p(t) & \dot{y}_p(t) \end{bmatrix}^T = \dot{s}(t)\,\mathbf{T}_r(t), \tag{25}$$

$$\dot{\varphi}_P(t) = \frac{\dot{s}(t)}{\rho(t)}. \tag{26}$$

Therefore, $\mathbf{q}_e(t) = \begin{bmatrix} q_L(t) & q_R(t) & x_P(t) & y_P(t) & \varphi_P(t) & q_1(t) \end{bmatrix}^T$ has been determined. Substituting $\mathbf{q}_e(t)$ and $\dot{\mathbf{q}}_e(t)$ into Eqs. (4)–(7) yields $\mathbf{M}(\mathbf{q}_e(t))$, $\mathbf{C}(\mathbf{q}_e(t), \dot{\mathbf{q}}_e(t))$, and $\mathbf{G}(\mathbf{q}_e(t))$.

Further, $\mathbf{S}(\mathbf{q}_e(t))$ is obtained from Eq. (9). Therefore, matrices $\mathbf{M}_n(\mathbf{q}_e(t))$, $\mathbf{C}_n(\mathbf{q}_e(t), \dot{\mathbf{q}}_e(t))$, and $\mathbf{G}_n(\mathbf{q}_e(t))$ can be also calculated.

Substituting $\mathbf{M}_n(\mathbf{q}_e(t))$, $\mathbf{C}_n(\mathbf{q}_e(t), \dot{\mathbf{q}}_e(t))$, $\mathbf{G}_n(\mathbf{q}_e(t))$, $\dot{\mathbf{q}}(t)$ and $\ddot{\mathbf{q}}(t)$ into Eq. (16) we evaluate the torque $\boldsymbol{\tau}(t)$.

Polynomial approximation and interpolation routines of Matlab Simulink are used for calculating $\mathbf{r}(u)$, $\mathbf{c}(u)$ and subsequently $\mathbf{r}(t)$, $\mathbf{c}(t)$. Eqs. (22), (23), (25) and (26) are evaluated symbolically using the "Integrator" and "Derivative" blocks of Simulink. The entire computational model designed as a real time Simulink model is shown in Fig. 3. Some additional script functions are embedded into the code to compute $\varphi_P(t)$ in Eq. (24), $\dot{\mathbf{q}}_w(t)$ in Eq. (20) and $q_1(t)$ in Eq. (22). The output of the algorithm are $\boldsymbol{\tau}(t)$ and $\boldsymbol{\lambda}(t)$ (see the bottom-left corner of Fig. 3). The calculation the constraint forces $\boldsymbol{\lambda}(t)$ is presented in the next section.
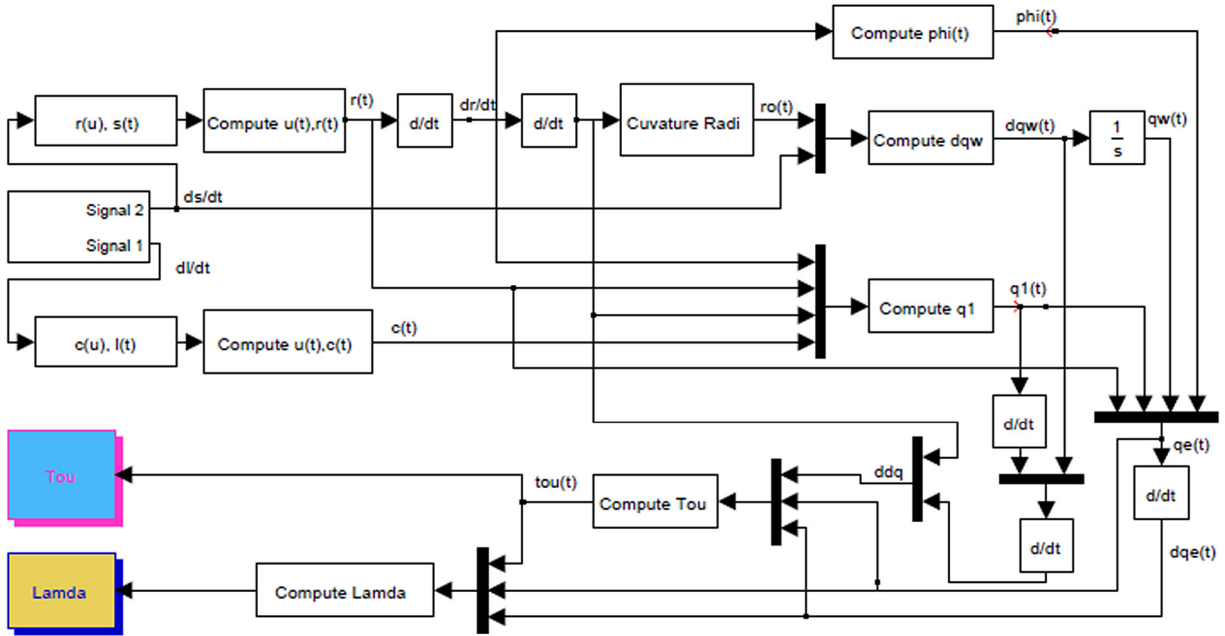
Fig. 3. Computational model using Simulink.

Example 1 (*Stationary Target*). The following parameters of the robot system are given: $m_P = 30$ kg, $m_S = 1$ kg, $m_R = m_L = 1$ kg, $R = 0.2$ m, $W = 1$ m, $H = 0.5$ m, $I_{Lx} = 2 \times 10^{-3}$ kg m^2, $I_{Lz} = 3 \times 10^{-3}$ kg m^2, $I_{Rx} = I_{Lx}$, $I_{Rz} = I_{Lz}$, $I_{Px} = 4 \times 10^{-2}$ kg m^2, $I_{Py} = 3 \times 10^{-2}$ kg m^2, $I_{Pz} = 3 \times 10^{-2}$ kg m^2, $I_{Sz} = 0.5 \times 10^{-3}$ kg m^2, and $g = 9.8$ m/s^2. The required velocity profile of the robot is given as $\dot{s}(0) = 0$ m/s, and $\dot{s}(t) = 0.5$ m/s for $t \geq 2$ s. Fig. 4 shows the simulation result when the target is stationary. In this case, the robot moves along the curve $\mathbf{r}(t)$ while the end-effector aims at the target. Figs. 5 and 6 depict $x_p(t)$, $y_p(t)$, $\varphi_P(t)$ and $q_1(t)$ which agree with the position/orientation of the platform and orientation of the end-effector.

Figs. 7 and 8 show $\tau_1(t)$, $\tau_L(t)$ and $\tau_R(t)$. The curve agrees with the characteristics of the motion. At the acceleration phase $0 < t < 2$ s considerably large values of torques are required to start up the motion. However, at the steady state, $t \geq 2$ s, the torques are small and their shape are consistent with the shape of the trajectory. Note that $\tau_L(t)$ is nearly symmetrical relative to $\tau_R(t)$ which matches the structural symmetry of the rear wheels.

Example 2 (*Moving Target*). The second case is illustrated in Fig. 9. The target is moving with the velocity $\dot{s}(t) = 0.5$ while the robot system tracks the target. The required torques are presented in Figs. 10 and 11. Naturally, the magnitude of the driving torques required for the steady state is much smaller than that for the acceleration stage.

4. Real time non-holonomic constraint forces/moment analysis

The non-holonomic constraint represented by $\mathbf{A}(\mathbf{q}_e)$ (Eq. (5)) implies a relationship between the forces $\lambda_1(t)$, $\lambda_2(t)$ and the moment $\lambda_3(t)$ (Fig. 12). The non-sliding case includes the opposite components $-\lambda_1(t)$, $-\lambda_2(t)$ and $-\lambda_3(t)$ acting on the surface. These pairs of forces and the moments characterize the interaction between the ground surface and the entire system. Note that $\lambda_1(t)$ and $\lambda_2(t)$ act along x_G and y_G, and the moment $\lambda_3(t)$ is defined around z_G.

Differentiating $\mathbf{A}(\mathbf{q}_e)\dot{\mathbf{q}}_e = 0$ yields

$$\mathbf{A}\ddot{\mathbf{q}}_e + \dot{\mathbf{A}}\dot{\mathbf{q}}_e = 0. \tag{27}$$

Multiplying $\mathbf{M}(\mathbf{q}_e)\ddot{\mathbf{q}}_e + \mathbf{C}(\mathbf{q}_e, \dot{\mathbf{q}}_e)\dot{\mathbf{q}}_e + \mathbf{G}(\mathbf{q}_e) = \boldsymbol{\tau}_e + \mathbf{A}^T(\mathbf{q}_e)\lambda$ by $\mathbf{A}\mathbf{M}^{-1}$ and taking into account Eq. (27) entails

$$\mathbf{A}\mathbf{M}^{-1}\mathbf{A}^T\lambda = \mathbf{A}\mathbf{M}^{-1}(\mathbf{C}\dot{\mathbf{q}}_e + \mathbf{G} - \boldsymbol{\tau}_e) - \dot{\mathbf{A}}\dot{\mathbf{q}}_e. \tag{28}$$
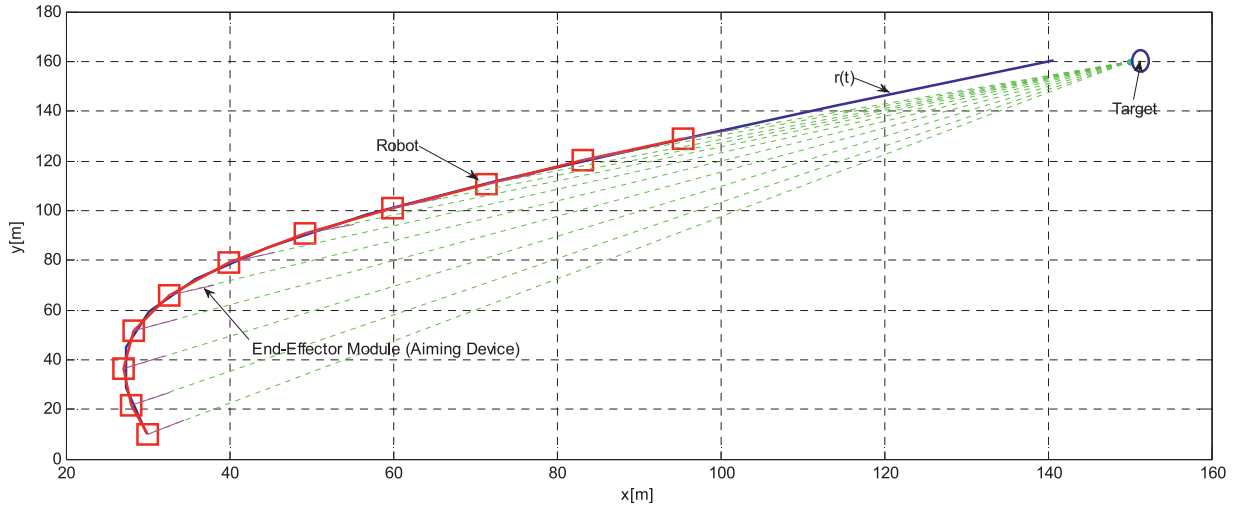
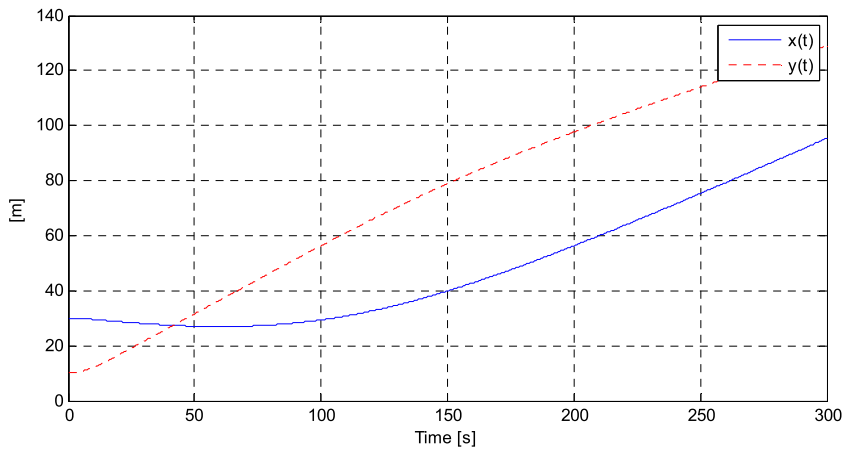**Fig. 4.** Position and orientation of the robot system (stationary target).

Fig. 5. Position of the mobile platform.
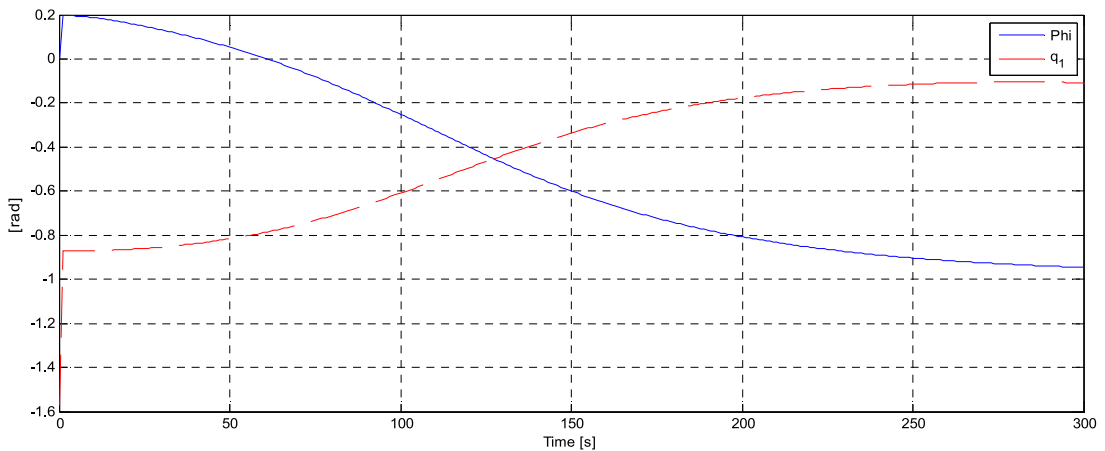

Fig. 6. Orientation of the platform and the end-effector.
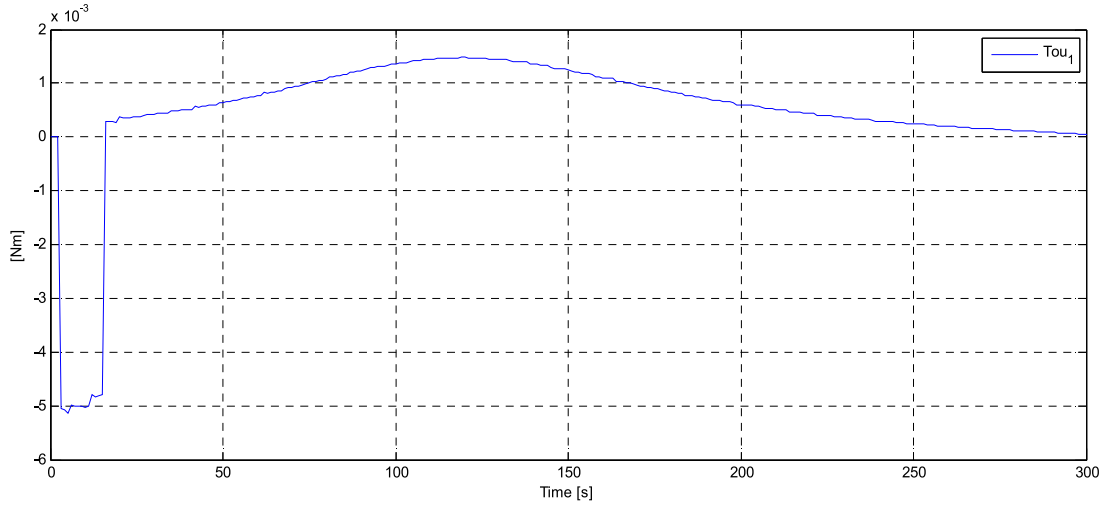
Fig. 7. Time evolution of $\tau_1(t)$ (stationary target).
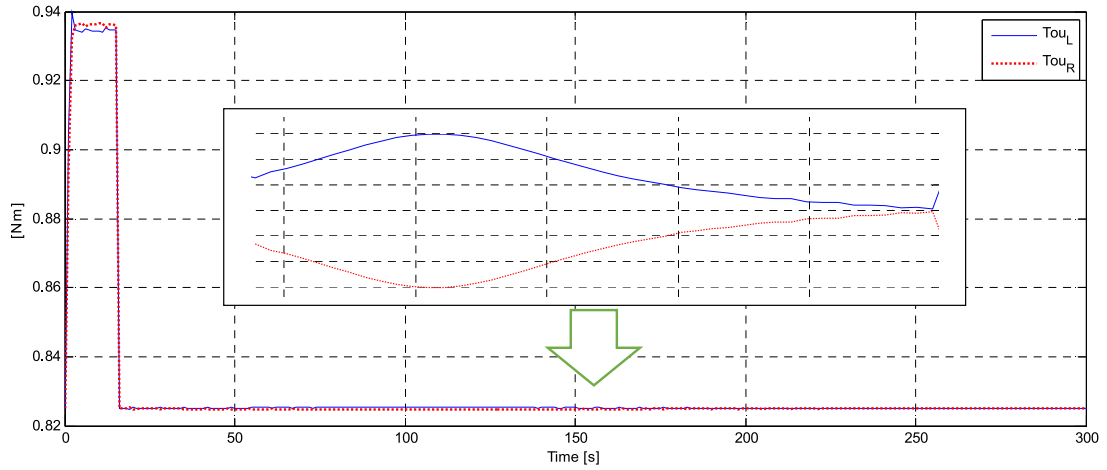

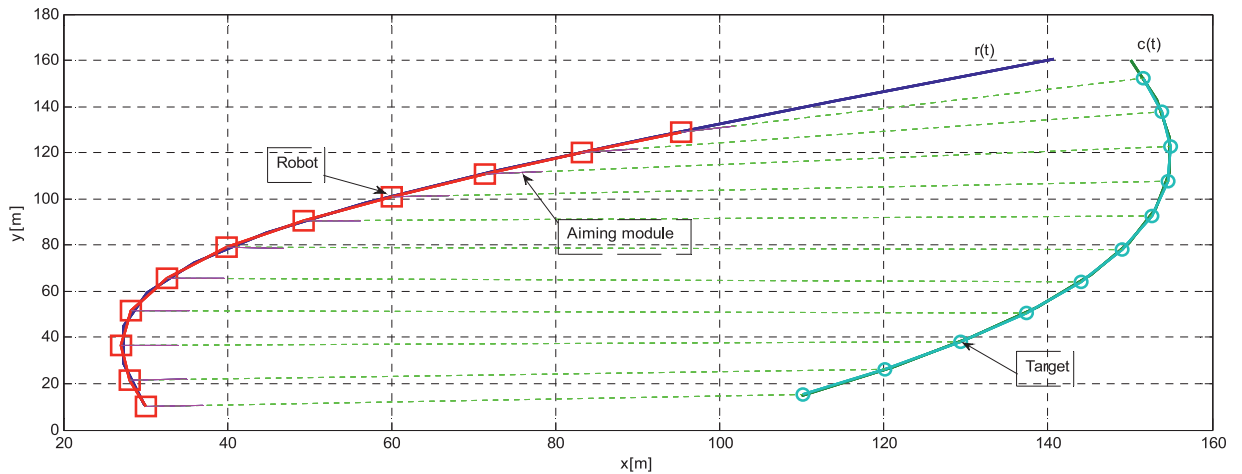**Fig. 8.** Time evolution of $\tau_L(t)$ and $\tau_R(t)$ (stationary target).

Fig. 9. Position and orientation of the robot system (moving target).
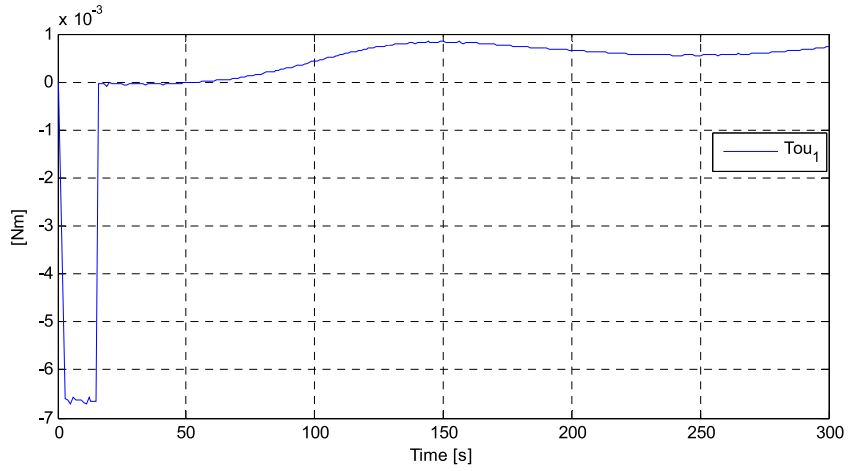
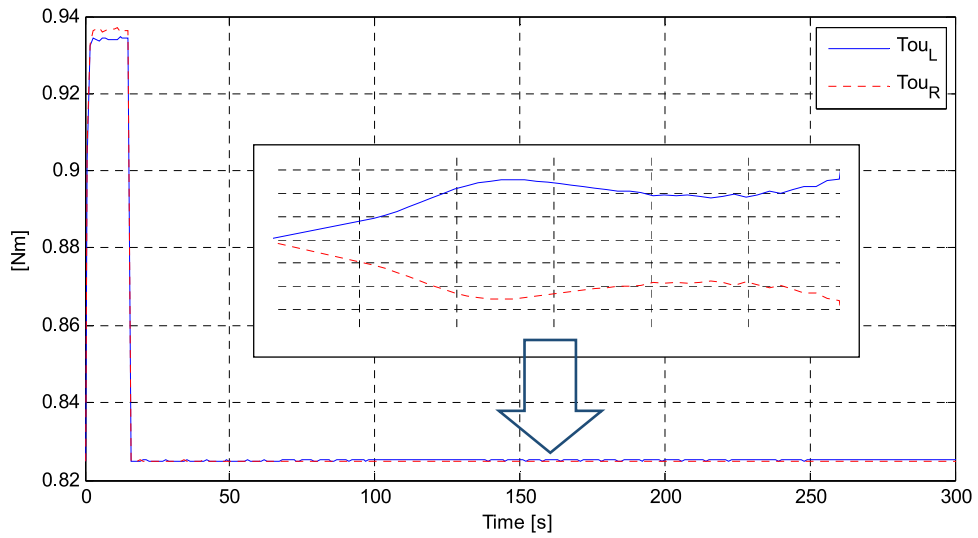**Fig. 10.** Time evolution of $\tau_1(t)$ (moving target).

Fig. 11. Time evolution of $\tau_L(t)$ and $\tau_R(t)$ (moving target).
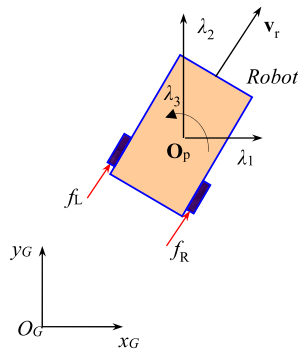

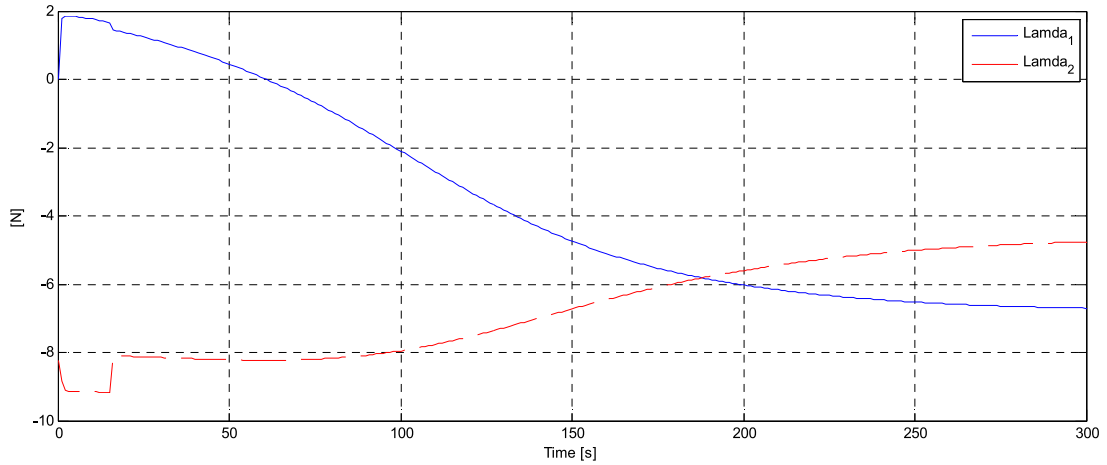**Fig. 12.** Non-holonomic constraint forces/moment.

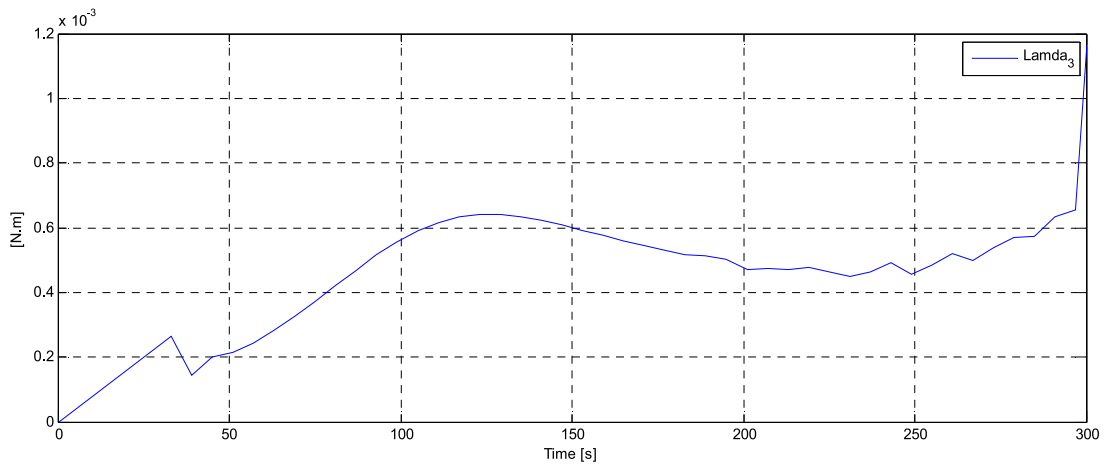**Fig. 13.** Time evolution of $\lambda_1(t)$ and $\lambda_2(t)$.

Fig. 14. Time evolution of $\lambda_3(t)$.

Assuming that $\det(\mathbf{A}\mathbf{M}^{-1}\mathbf{A}^T) \neq 0$ and solving (28) with regard to $\boldsymbol{\lambda}$ yields

$$\boldsymbol{\lambda} = \left(\mathbf{A}\mathbf{M}^{-1}\mathbf{A}^T\right)^{-1}\left(\mathbf{A}\mathbf{M}^{-1}\left(\mathbf{C}\dot{\mathbf{q}}_e + \mathbf{G} - \boldsymbol{\tau}_e\right) - \dot{\mathbf{A}}\dot{\mathbf{q}}_e\right). \tag{29}$$

Eq. (29) represents the desired relationship between the constraint forces/moment and parameters of the dynamic system such as the inertia, the mass, the geometry of the bodies, the required velocity, the external forces, the gravity, etc. It is combined with the calculations of the torques shown in Fig. 3 and solved numerically.

Consider the torque in the case when the target is moving (Fig. 9). The constraint forces and the moment calculated using Eq. (29) are shown in Figs. 13 and 14 respectively. Clearly, the magnitude of $\lambda_3(t)$ is quite small relative to $\lambda_1(t)$ and $\lambda_2(t)$. This complies with the behavior of the real physical system when the translational slip exceeds the turning slip.

Since $\boldsymbol{\lambda}(t) = \begin{bmatrix} \lambda_1(t) & \lambda_2(t) & \lambda_3(t) \end{bmatrix}^T$ characterizes the interaction between the system and the surface, their magnitude and direction significantly affect the instantaneous static balance between the wheels and the surface at the contact points

Recall Eq. (5). Clearly, $\mathbf{A}^T(\mathbf{q}_e)\boldsymbol{\lambda}$ is the "projection" of $\boldsymbol{\lambda}$ onto $\mathbf{q}_e = \begin{bmatrix} q_L & q_R & x_P & y_P & \varphi_P & q_1 \end{bmatrix}^T$. In other words, $\mathbf{A}^T(\mathbf{q}_e)\boldsymbol{\lambda}$ are components of the generalized forces corresponding to the non-holonomic constraint forces represented in he extended generalized coordinates. Therefore, in the generalized coordinates q_L and q_R, the actual

components of non-holonomic constraint forces are given by

$$f_L(t) = \frac{\lambda_1(t)\sin\varphi_p(t) - \lambda_2(t)\cos\varphi_p(t)}{2} + \frac{\lambda_3(t)}{W}, \tag{30}$$

$$f_R(t) = \frac{\lambda_1(t)\sin\varphi_p(t) - \lambda_2(t)\cos\varphi_p(t)}{2} - \frac{\lambda_3(t)}{W}. \tag{31}$$

Eqs. (30)–(31) represent the forces exerted on the driving wheels by the ground surface.

Denote $f_W^{Max} = \max(|f_L(t)|, |f_R(t)|)$. If f_W^{Max} is greater than the maximum value of the static friction force preventing the driving wheel from the sliding, the slipping occurs.

We approximate the static friction force applied to the wheels as follows

$$f_{Wf} = \frac{\mu_s g(m_1 + m_2 + m_3 + m_4)}{2}, \tag{32}$$

where μ_s is the coefficient of the static friction.

To keep the wheel rolling without slip, the following condition must be satisfied.

$$f_W^{Max} < f_{Wf}^{Max}. \tag{33}$$

Therefore,

$$\mu_s > \frac{2 f_W^{Max}}{g(m_1 + m_2 + m_3 + m_4)}. \tag{34}$$

Eq. (34) can be used to design the size and the material of the wheels to design the autonomous robots depending on their functional requirements.

Example 3 (*Selection of the Wheels*). Consider the mobile platform, of which the maximum velocity is required to reach 1 m/s, 1.5 m/s and 2 m/s, respectively. The non-holonomic constraint forces are computed as shown in Fig. 15, for $m = 30$ kg (robot mass), and in Fig. 16 for $m = 45$. Eq. (34) reveals that $m = 30$ requires that the friction coefficient $\mu_s > 0.1501$ for $v_{\max} = 2$, and $\mu_s > 0.101$ for $v_{\max} = 1.5$. The case $m = 45$, $v_{\max} = 2$ requires $\mu_s > 0.302$.

Finally, consider the rubber tired wheel and the pneumatic tire wheel to analyze whether their sliding resistance is applicable. The corresponding sliding friction coefficients for different surfaces are shown in Table 1 [14,21]. Symbols $-$ and $+$ denote acceptability of the wheels. Clearly, the rubber tired wheel can be used only for asphalt surface for if the maximum velocity is required as 2 m/s. However, if the maximum velocity downs to 1.5, and the mass of the robot is reduced to 30, it becomes a feasible option. The second type of wheel represents a better option for the robot in the example. The wheel is capable of moving on all the required surfaces except the snow.

5. Experiments

The experiments were designed and conducted for validation of the applied torques imposing on the wheels of an actual robot system. The experiments were conducted for the case of stationary target, and the robot was required to move along the trajectory as shown in Fig. 4.

The robot system and experimental set-ups are shown in Fig. 17. The system includes a robot, a control unit Arduino Atmega 2560, two DC Servo motors and Drivers (DCM50-775 24VDC 400RPM encoder 13ppr), one RC Servo motor, a Multifunction I/O Device USB NI 6002 and a Notebook Dell Intel Core i5. The parameters of the robot are given: $m_P = 8.7$ kg, $m_S = 0.7$ kg, $m_R = m_L = 0.4$ kg,

$R = 0.1$ m, $W = 0.42$ m, $H = 0.125$ m. The required velocity profile of the robot is given as $\dot{s}(0) = 0$ m/s, and $\dot{s}(t) = 1.5$ m/s for $t \geq 2$ s.

Based on the given geometric path $\mathbf{r}(u)$ in Fig. 4, the trajectory $\mathbf{r}(t)$ in the task space and the trajectory $\mathbf{q}(t) = \begin{bmatrix} q_L(t) & q_R(t) & q_1(t) \end{bmatrix}^T$ in the joint space are computed as the desired trajectory for the robot. The three motors driving the robot are controlled to operate with respect to the required trajectory $\mathbf{q}(t) = \begin{bmatrix} q_L(t) & q_R(t) & q_1(t) \end{bmatrix}^T$. The currents of the motors are measured and transformed into the applied torques imposing on the left and the right wheels of the robot. The applied torques by the experiments and by the simulation are shown in Fig. 18. It can be seen that the shape and the value of the simulation curves and the experimental readings are well matching, which shows a good validation of the proposed dynamic modeling and analysis results.
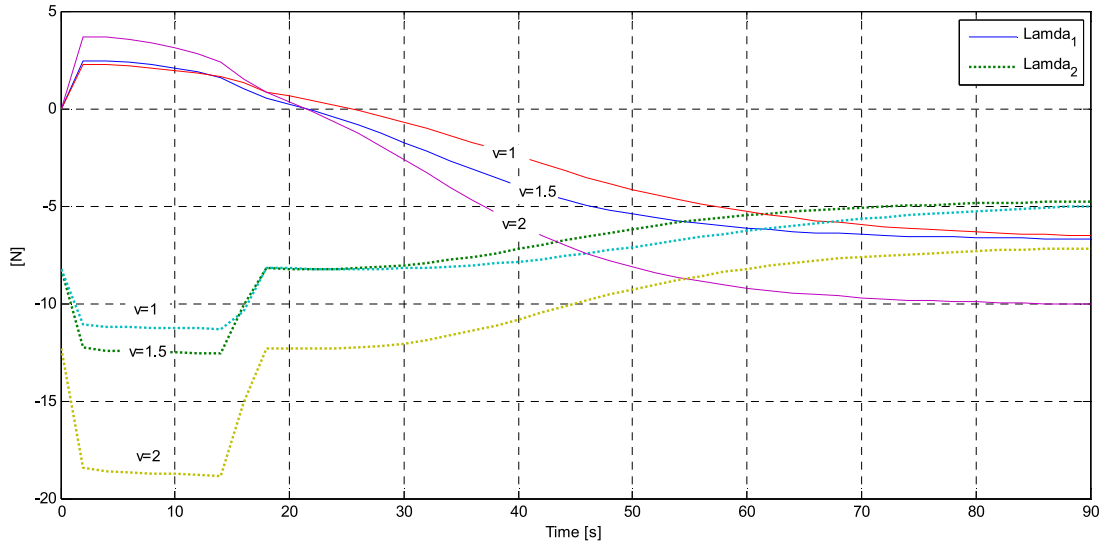
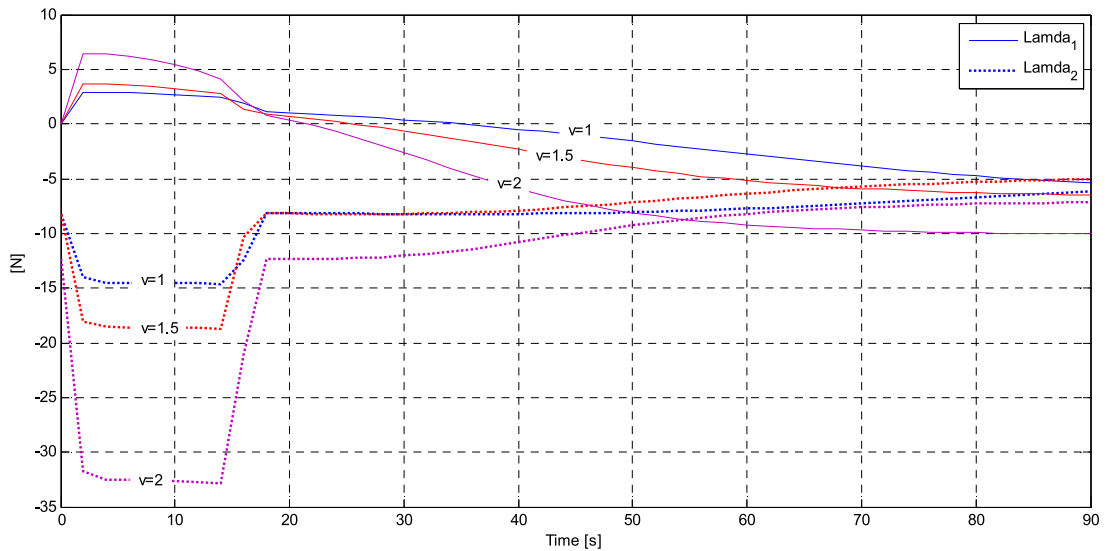**Fig. 15.** $\lambda_1(t)$ and $\lambda_2(t)$. Case: $m = 30$.

Fig. 16. $\lambda_1(t)$ and $\lambda_2(t)$. Case: $m = 45$.

6. Summary and conclusions

In this paper, the time varying torques and non-holonomic constraint forces that impose on a security robot system, with a wheeled mobile platform and a manipulator for special task applications, are mathematically modeled and analyzed. The efficient solutions for computation of these time varying torques and non-holonomic constraint forces were successfully developed for modeling and analysis of robot systems with the strongly coupled dynamics. The results of the numerical analysis of the torques fit well with the characteristics of the dynamic motion process of the specific system configuration in which the mobile platform moves on a real time smooth trajectory and the end-effector keeps aiming to a stationary/moving target. In the starting up phase, a big change of the torques are required to force the system approach to the velocity value as required, and the curves of the torques are shaped like square pulses which clearly reflect the increasing speed of the robot. In the steady state, the torques change smoothly and their shape are consistent with the shape of the trajectory; in particular, the torque $\tau_L(t)$ is nearly symmetrical

Table 1
The friction coefficient of the two wheel types on different surfaces.

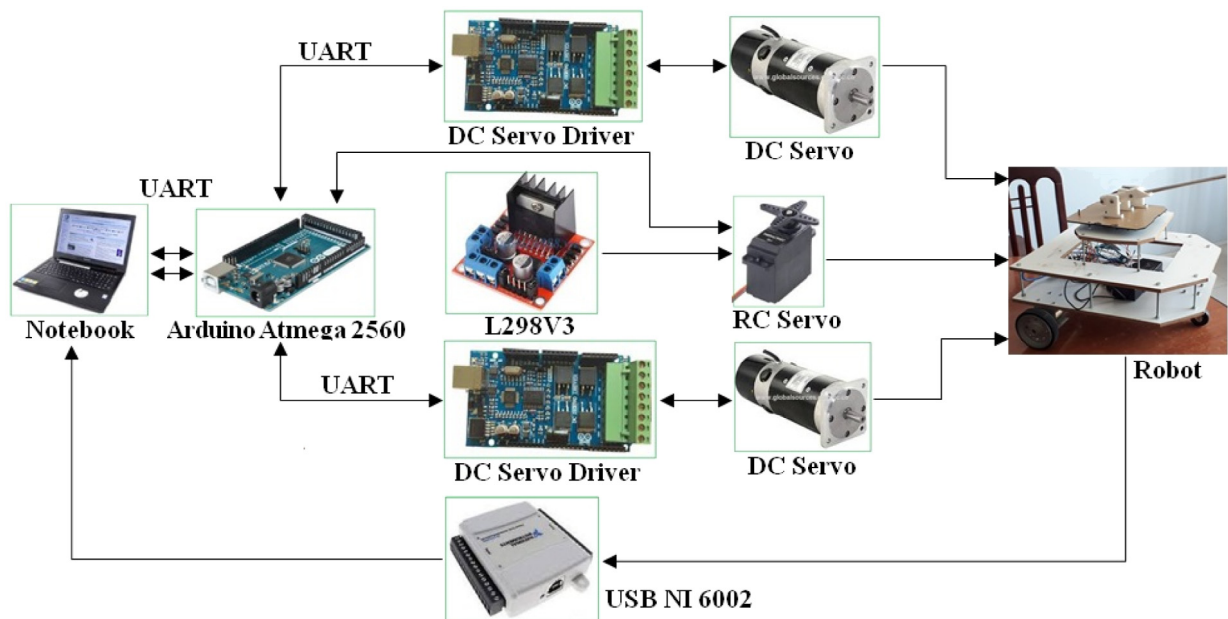|	Dry rough concrete	Wet grassy field	Wet dirt road	Wet–Dry asphalt	Snow
Rubber tired wheel	0.1	0.2	0.3	0.35–0.6	0.1–0.2
$m = 45$ $v_{max} = 2$	−	−	−	+	−
$m = 30$, $v_{max} = 1$	+	+	+	+	+
Pneumatic tire wheel	0.5–0.75	0.6	0.55–0.65	0.5–0.75	0.08–0.1
$m = 45$, $v_{max} = 2$	+	+	+	+	−

Fig. 17. Robot and experiment diagram.

to $\tau_R(t)$ that is suitable with the symmetrical feature of the structure design of the left and the right wheels. These specific results demonstrate the appropriateness and the effectiveness of the dynamic modeling presented in the minimal form in Eq. (16). This model is thus recommended as an alternative for the further development of control laws, instead of the model in the full description that has been mostly used. The proposed analysis methodology could be useful for simulating and investigating the dynamic behaviors of the alternatives of the robotic structure
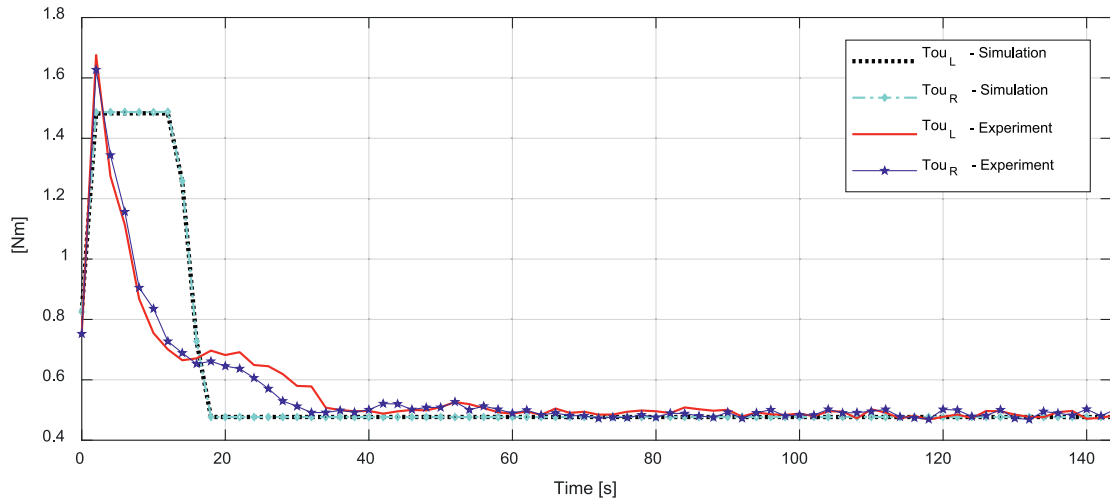
Fig. 18. Time evolution of $\tau_L(t)$ and $\tau_R(t)$ by simulation and by experiments (stationary target).

for improving the general system design. Especially, this is crucial for material selection, structural strength and geometric design of links, and for selecting suitable actuators.

The analysis of the non-holonomic constraint forces shows clearly what happen inside the interactions between the wheels and the motion surface. The required coefficient of static friction of the outer surface of the wheels can be calculated with Eq. (37). This result could lead to an important base for optimizing selection of the wheels to minimize the slippage, with respect to the functional requirements and traction condition of an autonomous robotic system.

Finally, the numerical examples and experiments were implemented to validate the proposed dynamic modeling method; and it clearly shows a close match about the results between the simulation and the experiment.

Acknowledgment

References

[1] I. Akli, B. Bouzouia, N. Achour, Motion analysis of a mobile manipulator executing pick-up tasks, Comput. Electr. Eng. 43 (2015) 257–269.
[2] G. Bayar, A.B. Koku, E. Ilhan Konukseven, Dynamic modeling and parameter estimation for traction, rolling, and lateral wheel forces to enhance mobile robot trajectory tracking, Robotica 33 (10) (2015) 2204–2220.
[3] A. Dietrich, K. Bussmann, F. Petit, P. Kotyczka, C. Ott, B. Lohmann, A. Albu-Schäffer, Whole-body impedance control of wheeled mobile manipulators, Auton. Robots 40 (3) (2016) 505–517.
[4] W. Dong, On trajectory and force tracking control of constrained mobile manipulators with parameter uncertainty, Automatica 38 (2002) 1475–1484.
[5] M. Fruchard, P. Morin, C. Samson, A framework for the control of nonholonomic mobile manipulators, Int. J. Robot. Res. 25 (8) (2006) 745–780.
[6] M. Galicki, Two-stage constrained control of mobile manipulators, Mech. Mach. Theory 54 (2012) 18–40.
[7] M. Galicki, Constrained finite-time control of mobile manipulators, Procedia Eng. 96 (2014) 111–125.
[8] M. Galicki, Real-time constrained trajectory generation of mobile manipulators, Robot. Auton. Syst. 78 (2016) 49–62.
[9] K. Izumi, K. Watanabe, Fuzzy behavior-based control trained by module learning to acquire the adaptive behaviors of mobile robots, Math. Comput. Simulation 51 (3–4) (2000) 233–243.
[10] R. Joanna, T. Krzysztof, Dynamically consistent Jacobian inverse for mobile manipulators, Internat. J. Control 89 (2016) 1159–1168.
[11] A. Khalil, S.A.A. Moosavian, Dynamically stable motion planning of wheeled robots for heavy object manipulation, Adv. Robot. 29 (8) (2015) 545–560.
[12] M.H. Korayem, A.M. Shafei, Motion equation of nonholonomic wheeled mobile robotic manipulator with revolute-prismatic joints using recursive Gibbs-Appell formulation, Appl. Math. Model. 39 (5) (2015) 1701–1716.
[13] Z. Li, W. Chen, H. Liu, Robust control of wheeled mobile manipulators using hybrid joints, Int. J. Adv. Robot. Syst. 5 (1) (2008) 83–90.

[14] C.Y. Lin, C.C. Hsu, C.P. Fung, The study of coefficient of friction for light motorcycle sliding on asphalt road, Int. J. Phys. Sci. ap 7 (30) (2012) 5167–5174.

[15] Y. Liu, Y. Li, Dynamic modeling and adaptive neural-fuzzy control for nonholonomic mobile manipulators moving on a slope, Int. J. Control Autom. Syst. 4 (2) (2006) 197–203.

[16] M. Mailah, E. Pitowarno, H. Jamaluddin, Robust motion control for mobile manipulator using resolved acceleration and proportional-integral active force control, Int. J. Adv. Robot. Syst. 2 (2) (2005) 125–134.

[17] Mazur, Trajectory tracking control in workspace-defined tasks for nonholonomic mobile manipulators, Robotica 28 (1) (2010) 57–68.

[18] S. Mishra, P.S. Londhe, S. Mohan, S.K. Vishvakarma, B.M. Patre, Robust task-space motion control of a mobile manipulator using a nonlinear control with an uncertainty estimator, Comput. Electr. Eng. 67 (2018) 729–740.

[19] V. Padois, J.Y. Fourquet, P. Chiron, Kinematic and dynamic model-based control of wheeled mobile manipulators: a unified framework for reactive approaches, Robotica 25 (2) (2007) 157–173.

[20] J. Peng, J. Yu, J. Wang, Robust adaptive tracking control for nonholonomic mobile manipulator with uncertainties, ISA Trans. 53 (4) (2014) 1035–1043.

[21] B.N.J. Persson1, U. Tartaglino, O. Albohr, E. Tosatti, Rubber friction on wet and dry road surfaces: the sealing effect, Phys. Rev. B 71 (3) (2005) 035428.

[22] Y. Qing, C. I-Ming, A general approach to the dynamics of nonholonomic mobile manipulator systems, J. Dyn. Syst. Meas. Control 124 (2002) 513–521.

[23] G.G. Rigatos, Extended Kalman and particle filtering for sensor fusion in motion control of mobile robots, Math. Comput. Simulation 81 (3) (2010) 590–607.

[24] J. Tan, N. Xi, Y. Wang, Integrated task planning and control for mobile manipulators, Int. J. Robot. Res. 22 (5) (2002) 337–354.

[25] M. Tounsi, J.F. Le Corre, Trajectory generation for mobile robots, Math. Comput. Simulation 41 (3–4) (1996) 367–376.

[26] C.M. Wronka, M.W. Dunnigan, Derivation and analysis of a dynamic model of a robotic manipulator on a moving base, Robot. Auton. Syst. 59 (2011) 758–769.

[27] X. Wu, Y. Wang, X. Dang, Robust adaptive sliding-mode control of condenser-cleaning mobile manipulator using fuzzy wavelet neural network, Fuzzy Sets and Systems 235 (2014) 62–82.

[28] K. Xia, H. Gao, L. Ding, G. Liu, Z. Deng, Z. Liu, C. Ma, Trajectory tracking control of wheeled mobile manipulator based on fuzzy neural network and extended Kalman filtering, Neural Comput. Appl. 30 (2) (2018) 447–462.

Chu A. My received the M.Eng. and Dr.Eng. degrees in Industrial Systems Engineering from Asian Institute of Technology, Thailand in 2001 and 2005, respectively. He was an Assistant Professor (2005), and Associate Professor (2011) with Department of Special Robotics and Mechatronics, Le Quy Don Technical University, Hanoi, Vietnam.

Stanislav S. Makhanov received the M.Sc. degree in Applied Mathematics from the Moscow State University in 1981 and the Dr. Sc degree from the Computing Center of the Russian Academy of Science in 1988, where he worked as an Associate Professor until 1993. From 1994 to 1999, he was a Visiting Professor with King Mongkut's Institute of Technology, Ladkrabang and Associated Faculty with the Asian Institute of Technology of Thailand. He is currently a Full Professor and a Head of a Center of Biomedical Engineering with Sirindhorn International Institute of Technology, Thammasat University of Thailand.

Nguyen A. Van received the M.Sc. and Ph.D. degrees in Robotics from the Moscow State University, Russia in 2009 and 2015, respectively. He is currently a Lecturer and Vice Head at Department of Special Robotics and Mechatronics, Le Quy Don Technical University, Hanoi, Vietnam.

Vu M. Duc received the B.Eng. and M.Eng. degrees in Mechatronics from the Hanoi University of Science and Technology, Hanoi, Vietnam in 2005 and 2011, respectively. He is currently a Lecturer at Department of Special Robotics and Mechatronics, Le Quy Don Technical University, Hanoi, Vietnam.